
Modeling Depth Ambiguity: A Mixture-Density Representation for Flying-Point-Free Depth Estimation

Siyuan Bian^{1*} Congrong Xu^{1*} Jun Gao^{1,2}

¹University of Michigan ²NVIDIA
{siyuanb, xucr, jungaocv}@umich.edu

*Equal contribution.

Abstract

Despite advances in depth estimation, *flying points* remain a persistent failure mode: near object boundaries, depth estimators often predict spurious 3D points in the empty space between foreground and background surfaces. We trace this artifact to a standard modeling choice: assigning each pixel a single depth hypothesis. At boundaries, a pixel can straddle a foreground and a background surface, so its true depth is ambiguous between the two. A model that predicts a single depth cannot keep both possibilities, so training instead pulls the prediction toward an intermediate depth that lies on neither surface. We address this with MDA, a mixture-density representation that lets the model predict multiple depth hypotheses and their associated probabilities for each pixel. Near boundaries, different hypotheses can align with different surfaces, and the decoded depth is selected from one of these hypotheses rather than placed in the empty space between them. Across different backbones, MDA substantially improves boundary reconstruction and largely removes flying-point artifacts even under severe input blur, while adding negligible runtime overhead. The same mixture-density framework naturally extends to transparent objects, where it predicts multiple depth layers at transparent pixels, and to sky regions, where a dedicated component separates the unbounded sky from finite-depth regions, producing flying-point-free skylines. Project Page: <https://biansy000.github.io/mda-site/>.

1 Introduction

Depth estimation from images has advanced remarkably in recent years [6, 13, 24, 32, 28]: feed-forward models can now recover accurate depth from a single frame or a handful of views. Yet one common failure remains widespread: *flying points*, 3D points that fall in empty space between foreground and background surfaces near object boundaries (Fig. 1). These artifacts corrupt reconstructed geometry and reduce the reliability of downstream applications such as novel-view synthesis and robotic manipulation. Importantly, flying points persist despite stronger backbones [13, 24] and larger training datasets [37, 14, 16, 27, 20], suggesting that they are not simply a scaling problem.

We argue that flying points arise from a seemingly natural modeling choice: most depth estimators assign each pixel only one depth hypothesis. This works well on ordinary pixels, but becomes problematic at object boundaries. A boundary pixel can straddle an occlusion edge, so its image patch and features contain cues from both the foreground and background, making it difficult for the model to determine which surface the pixel belongs to. In reality, the correct point should lie on either the foreground or background surface, not between them. However, when the model is trained to predict a single value, it tends to compromise between the two plausible surface depths, producing a point in empty space. This limitation is also reflected in the training objective. Standard

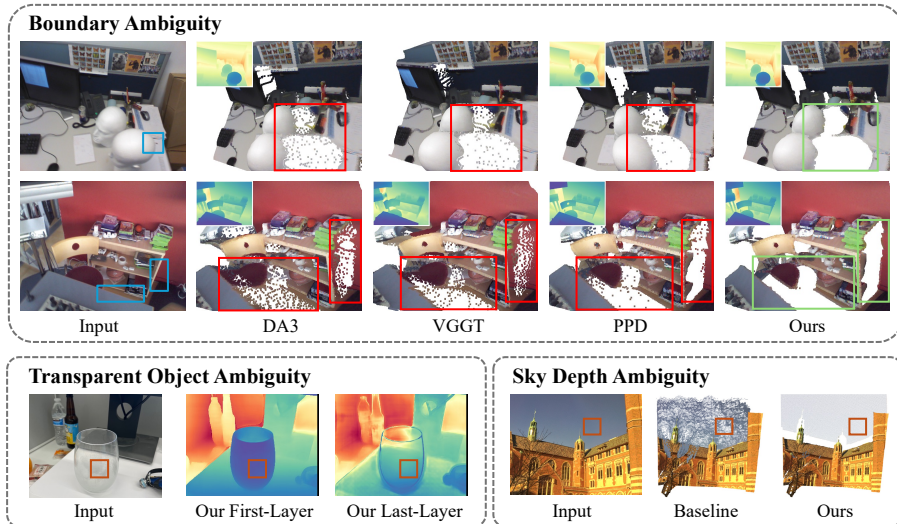


Figure 1: Overview of our approach. Existing depth estimators model each pixel as a unimodal distribution, producing flying-point artifacts at boundaries. Our mixture-density model maintains multiple depth hypotheses, eliminating boundary artifacts, recovering layered depth behind transparent objects, and providing a clean skyline.

ℓ_1 and ℓ_2 depth losses are negative log-likelihoods of Laplacian or Gaussian distributions centered at the predicted depth, thereby enforcing a unimodal per-pixel representation. This representation is well matched to smooth, unambiguous surfaces, but too restrictive at boundaries, where the plausible depth distribution is naturally multi-modal.

Prior work on flying points has not analyzed this underlying cause, and existing fixes are therefore only partial. PPD and PPVD [31, 32] use generative models to refine the outputs of feed-forward depth estimators, but their multi-step denoising process is slow and struggles when input images are blurry (Fig. 7). MoE3D [29] routes different spatial regions to different depth heads but is still trained under a single-depth objective, so boundary ambiguity is re-distributed in different experts rather than resolved. SMDNet [23] proposed a two-component Laplacian mixture loss, but only focused on stereo disparity estimation rather than monocular depth, and without theoretical motivation.

To address this issue, we propose Modeling Depth Ambiguity (MDA), a mixture-density depth representation that explicitly models the depth ambiguity near the boundary. For each pixel, the model predicts K Laplacian or Gaussian depth hypotheses together with their probabilities, and is trained with the corresponding mixture negative log-likelihood. On ordinary pixels, these hypotheses can agree, behaving like the original unimodal representation; near boundaries, they can instead represent the foreground and background surfaces separately. In this way, ambiguity is represented by probabilities over multiple depth hypotheses, rather than by shifting a single depth prediction into empty space. During training, different components specialize to different depth layers and remain anchored to valid surfaces. At inference, the decoded depth is selected from these hypotheses, so even imperfect boundary probabilities still yield points on existing surfaces instead of between surfaces.

MDA keeps the backbone unchanged and only modifies the final prediction layer: each component predicts a depth, a confidence score (§3.1), and a mixture-weight logit. It therefore adds only a small number of output channels and negligible inference overhead. We instantiate our representation on two depth estimators, DA3 and VGGT. With minimal changes to either model, our approach substantially improves boundary reconstruction quality (Fig. 5) and removes flying points in the vast majority of scenes, even when the input is heavily blurred (Fig. 7).

Our mixture-density representation extends beyond object boundaries to broader forms of *depth ambiguity*, where a single pixel cannot be explained well by one depth value. For transparent objects, a camera ray may pass through glass and intersect multiple visible surfaces, making multiple depths physically valid at the same pixel. We adapt our representation so that multiple hypotheses can be active simultaneously, allowing the model to recover co-existing depth layers in transparent regions while preserving sharp boundaries elsewhere. For sky regions, where depth is effectively unbounded, we add a dedicated large-depth component. This yields threshold-free sky segmentation and clean, flying-point-free skylines within the same prediction framework.

In summary, our contributions are:

- We identify flying points as a consequence of forcing depth estimators to predict a single depth value at ambiguous boundary pixels.
- We propose a lightweight K -component mixture-density depth representation that predicts multiple depth hypotheses and their probabilities, allowing boundary pixels to choose between foreground and background surfaces instead of averaging between them.
- We show that this representation can be applied to both DA3 and VGGT, improves boundary reconstruction, removes flying points in most scenes, and naturally extends to transparent objects and sky regions.

2 Related Work

Monocular and Multi-View Depth Estimation. Early work on monocular depth estimation leveraged deep CNN regressors [6] for single-image depth prediction. Subsequent work improved cross-dataset generalization (MiDaS [18]), adopted Vision Transformers for dense prediction (DPT [19]), and scaled the paradigm to billions of unlabeled images [33, 34]. More recently, researchers extended single-image depth estimation to multiple frames or views. DUST3R [26] introduced a fully feed-forward framework for multi-view reconstruction, and MAST3R [12] built on this foundation with 3D-aware feature matching for better multi-view accuracy. VGGT [24], Pi-3 [28], MapAnything [10], and Depth Anything 3 [13] take this further by jointly predicting camera parameters, depth maps, or dense 3D points in a single transformer forward pass over arbitrary image collections. However, all these methods employ the unimodal depth modeling, limiting their ability to represent depth ambiguity at boundaries, transparent surfaces, and sky.

Depth Ambiguity at Boundaries, Transparent Surfaces, and Sky. Depth ambiguity manifests most severely at object boundaries, where flying points corrupt downstream tasks, and several methods have attempted to address it directly. Pixel-Perfect-Depth [31, 32] uses a pixel-space Diffusion Transformer to refine the output of feed-forward depth estimators to generate sharp boundaries. MoE3D [29] uses a mixture-of-experts architecture to route spatial regions to specialized depth heads and is trained with a unimodal L2 loss. These methods leave many flying points unresolved, especially on blurry inputs. SMDNet [23] is the closest in spirit to our formulation, modeling stereo disparity as a two-component Laplacian mixture, but it is restricted to stereo, lacks a theoretical motivation, and does not extend to transparent surfaces or sky.

Depth ambiguity also arises on transparent surfaces, where multiple depths co-exist along a single ray. The Booster dataset [17] exposes the limitations of standard stereo methods on transparent and reflective materials; ClearGrasp [21] addresses transparent-object depth for robotic manipulation; and LayeredDepth [30] introduces the first benchmark with multi-layer depth annotations. Despite these efforts, depth estimation for transparent objects remains a challenge. Sky pixels, whose true depth is effectively infinite, are typically handled outside the depth pipeline: Depth Anything 3 [13], for example, treats sky as a separate segmentation problem, training a dedicated network alongside its depth estimator.

3 Methods

The introduction motivates our main idea: boundary pixels should be represented by multiple surface-valued depth hypotheses rather than by a single averaged depth. We now formalize this idea. We first show that the standard confidence-weighted depth loss corresponds to a unimodal likelihood (§3.1). We then replace this likelihood with a mixture-density representation that predicts multiple hypotheses and their probabilities (§3.2). Finally, we describe decoding, architecture, and the Gaussian-mixture variant used in our experiments.

3.1 Preliminary: Unimodal Depth Representation and Its Limitations

Modern depth estimators such as DA3 [13] and VGGT [24] predict, for each pixel i , a depth \hat{D} and a confidence C^D . The network is trained to minimize confidence-weighted L1 loss over all N pixels:

$$\mathcal{L}_{\text{Depth}} = \sum_{i=1}^N \left(C^D \| \hat{D} - D \|_1 - \alpha \log C^D \right), \quad (1)$$

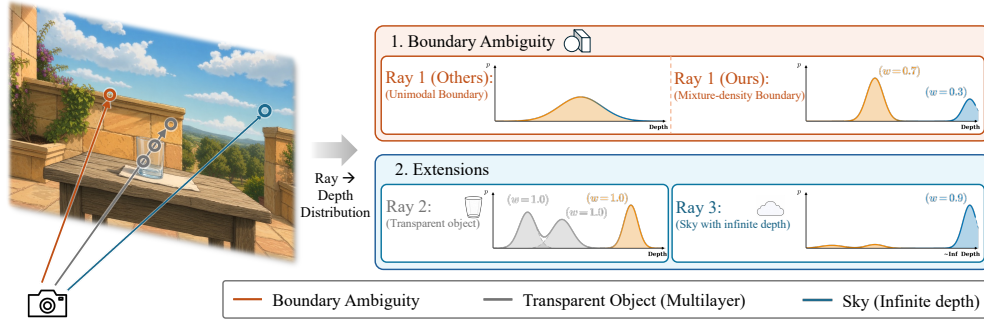


Figure 2: Three forms of depth ambiguity. **Ray 1 (Boundary)**: the pixel straddles a foreground edge and a background surface, producing two depth hypotheses whose relative mixture weights encode the model’s belief on which surface dominates. **Ray 2 (Transparent object)**: the ray physically intersects multiple surfaces (e.g., the two sides of a glass cup and the background wall), and all of them are simultaneously valid depths. **Ray 3 (Sky)**: the ray hits the sky (infinite depth in the end).

where D is the ground-truth depth and $\alpha > 0$ prevents the trivial solution $C^D = 0$.

This loss has a probabilistic interpretation. Assume the ground-truth depth at pixel i follows a Laplacian distribution centered at the depth prediction \hat{D} with a learned scale b , the probability of ground truth depth is: $p(D | \hat{D}, b) = \frac{1}{2b} \exp(-|\hat{D} - D|/b)$. With the reparameterization $C^D = \alpha/b$, the negative log-likelihood reduces to Eq. 1 up to a positive scale and an additive constant. Thus, the standard objective induces a unimodal per-pixel depth representation. The Gaussian case analogously yields a confidence-weighted ℓ_2 loss. Full derivations are provided in Appendix §A.1 and §A.2.

Reason from a Unimodal Representation to Flying Points. This formulation explains the limitation of standard depth regression: each pixel is represented by one distribution centered at one depth. This is appropriate on smooth regions, but not at boundaries. Consider a boundary pixel that straddles a foreground surface at depth d_{fg} and a background surface at depth d_{bg} , with $d_{bg} \gg d_{fg}$. Its RGB observation and deep features can contain information from both surfaces, making the surface assignment ambiguous for the model. A unimodal predictor must nevertheless explain the pixel with one depth value. Under this ambiguity, supervision pulls the prediction toward a compromise between d_{fg} and d_{bg} , which lies in empty space and becomes a flying point (Fig. 3, left).

3.2 Mixture-Density Depth Representation (MDA)

We replace the unimodal depth representation with a mixture-density representation that explicitly accounts for depth ambiguity (Fig. 3, right). Instead of requiring one predicted depth to explain every pixel, the model predicts multiple plausible depth hypotheses together with their probabilities. For each pixel, the prediction head outputs K depth hypotheses $\{\hat{D}_k\}_{k=1}^K$, scales $\{b_k\}_{k=1}^K$, and mixture weights $\{\pi_k\}_{k=1}^K$ with $\sum_{k=1}^K \pi_k = 1$ and $\pi_k \geq 0$. The mixture weights are produced by a softmax over per-component logits. The depth distribution can then be represented by:

$$p(D | \{\hat{D}_k, b_k, \pi_k\}_{k=1}^K) = \sum_{k=1}^K \pi_k \cdot \frac{1}{2b_k} \exp\left(-\frac{|\hat{D}_k - D|}{b_k}\right). \quad (2)$$

Each component represents one depth hypothesis. On ordinary pixels, all hypotheses may agree on the same surface. At boundaries, different hypotheses can specialize to different surfaces, e.g., foreground and background, while the mixture weights encode which surface is more likely.

Loss Derivation. Assuming independence across pixels, the training objective is the negative log-likelihood of the mixture density from Eq. 2 summed over all N pixels. We re-use the confidence reparameterization $C_k^D = \alpha/b_k$ from the unimodal case, and define a per-component loss $\mathcal{L}_k^{\text{Laplace}} = C_k^D |\hat{D}_k - D| - \alpha \log C_k^D$, which is exactly the loss of unimodal Laplacian (Eq. 1) applied to component k . Substituting everything into the mixture NLL and dropping constants yields (see the Appendix §A.1 for the full derivation):

$$\mathcal{L}_{\text{Mix}} = - \sum_{i=1}^N \log \sum_{k=1}^K \exp\left(\log \pi_k - \frac{1}{\alpha} \mathcal{L}_k^{\text{Laplace}}\right). \quad (3)$$

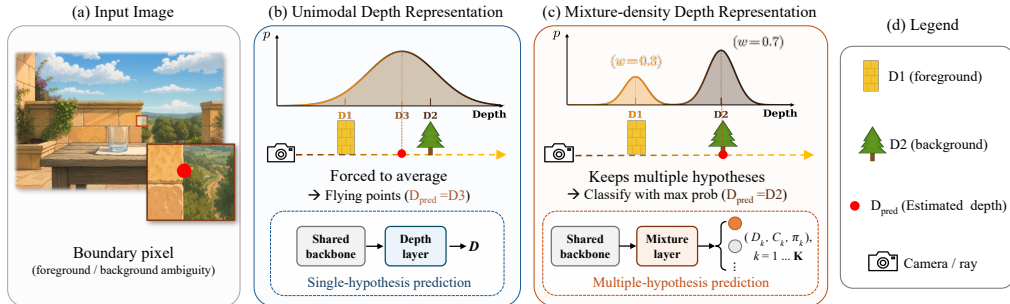


Figure 3: Unimodal versus mixture-density depth at an object boundary. (a) A boundary pixel may mix foreground and background evidence along the camera ray. (b) A unimodal predictor must output one depth, often averaging the foreground (d_1) and background (d_2) hypotheses into an intermediate estimate (d_3) that becomes a flying point. (c) Our mixture-density representation keeps multiple hypotheses and turns decoding into a selection among candidate surface depths, producing a boundary-aligned prediction.

This representation naturally generalizes the unimodal case: when $K = 1$ with a single Laplace component, Eq. 3 reduces to Eq. 1.

3.3 Decoding Without Averaging

The mixture distribution represents several plausible depth hypotheses, but downstream applications usually require a single decoded depth map. At inference, we therefore select the component whose predicted depth is most likely under the learned mixture distribution. Concretely, for each candidate depth \hat{D}_k , we evaluate its density under Eq. 2 and choose the candidate with the highest score:

$$k^* = \operatorname{argmax}_{k \in \{1, \dots, K\}} \sum_{j=1}^K \frac{\pi_j}{2b_j} \exp\left(-\frac{|\hat{D}_k - \hat{D}_j|}{b_j}\right), \quad \hat{d} = \hat{D}_{k^*} \quad (4)$$

This requires only K density evaluations with nearly negligible overhead.

Discussion on Flying Points. At a boundary pixel, different mixture components can represent different candidate surfaces: one may explain the foreground depth, while another explains the background depth. At inference, even if the model is uncertain about which surface the pixel belongs to, the decoded depth is selected from the learned hypotheses. The output therefore lies on one of the candidate surfaces instead of floating between them. Appendix §A.4 provides a detailed gradient analysis to support this.

Discussion with MoE3D [29]. Our representation modifies the last layer of the depth predictor to produce per-component predictions and supervises them with our mixture NLL loss. This design has two entangled factors of improvement: higher network capability with additional predictions and our representation with mixture-density. Close to our work, MoE3D [29] predicts multiple depths and averages them via softmax. Yet, MoE3D trains the model via a unimodal loss on the averaged depth, without mixture-density representation. We therefore compare with MoE3D and ablate the improvements in §5.1.3. The architectural change accounts for only a small portion of the improvement, while the mixture representation is the main driving force, demonstrating the effectiveness of our representation.

3.4 Extension to a Gaussian Mixture Model

The Laplacian mixture above can be directly extended to a Gaussian Mixture Model (GMM) by replacing each Laplace component with a Gaussian distribution. The mixture NLL retains the same form as Eq. 3, with the per-component ℓ_1 term replaced by an ℓ_2 term; the full derivation is in §A.2. For training stability we apply the Gaussian mixture in log-depth space, following previous work [31, 10] (details in §A.3). All other design choices remain unchanged.

In our experiments, we find that the Gaussian Mixture Model consistently outperforms the Laplacian Mixture Model on most benchmarks (see §5.1.3), likely because the ℓ_2 penalty provides stronger gradient signal for depth predictions at boundary areas and for non-dominant components. We therefore adopt the GMM as our default model unless otherwise stated.

Table 1: Boundary quality analysis. DA3+Ours and VGGT+Ours cut boundary error over every baseline across all three datasets and run $\sim 80\times$ faster than diffusion-based PPD / PPVD.

Method	NRGBD				7Scenes				HiRoom				FPS \uparrow
	Img		Seq		Img		Seq		Img		Seq		
	Acc \downarrow	CD \downarrow	Acc \downarrow	CD \downarrow	Acc \downarrow	CD \downarrow	Acc \downarrow	CD \downarrow	Acc \downarrow	CD \downarrow	Acc \downarrow	CD \downarrow	
PPD [31]	74.0	81.0	68.0	61.0	53.0	63.5	54.0	60.0	81.0	89.0	81.0	65.0	0.44
PPVD [32]	107.0	125.0	101.0	80.5	60.0	73.0	65.0	70.0	124.0	91.0	141.0	87.5	1.17
VGGT [24]	60.0	62.0	54.0	53.0	41.0	57.5	43.0	56.5	58.0	59.5	54.0	48.0	33.43
DA3 [13]	57.0	50.0	51.0	43.5	41.0	50.0	42.0	48.5	42.0	40.0	38.0	32.0	36.78
VGGT + Ours	28.0	38.0	27.0	34.0	35.0	42.0	37.0	42.5	45.0	50.0	42.0	40.5	34.11
DA3 + Ours (LMM)	25.0	<u>35.5</u>	22.0	29.5	<u>37.0</u>	<u>42.0</u>	38.0	<u>42.0</u>	31.0	<u>34.5</u>	29.0	28.0	33.32
DA3 + Ours (GMM)	25.0	35.0	<u>24.0</u>	<u>30.5</u>	35.0	40.5	36.0	40.5	31.0	34.0	<u>30.0</u>	28.0	33.32

4 Extensions to Other Depth Ambiguities

Our representation can be extended to other forms of depth ambiguities with minimal modifications. We study two forms of ambiguities in our paper: (I). Images of transparent objects (Fig. 2), where a pixel might indicate both the foreground glass and the background surface; (II). Images with sky (Fig. 2), where sky induces a special type of boundary. Sky pixels have infinite depth, which cannot be meaningfully represented by standard regressors, leading to severe depth discontinuities and flying-point artifacts at skylines.

4.1 Multi-Layer Depth for Transparent Objects

For transparent objects, a ray passing through glass physically intersects multiple surfaces. A pixel may therefore require multiple valid depth predictions: one for the visible transparent surface and another for the background behind it.

From Softmax to Sigmoid. The softmax mixture used for ordinary boundaries assumes that each pixel has one selected depth, since its weights are constrained to sum to one and the final prediction is decoded by selecting one component. To support transparent objects, we replace the softmax over mixture-weight logits with independent sigmoid weights, $\pi_k = \sigma(\pi'_k) \in (0, 1)$, so components are weighted independently rather than normalized against one another. Transparent pixels can then activate multiple components simultaneously, expressing co-existing depth layers along the ray. Opaque pixels are regularized to keep the weight sum close to one, retaining the boundary-handling behavior of the softmax variant.

Training and Inference. For simplicity, we set $K=2$ in this variant, modeling only two depth layers — the visible transparent surface and the background behind it. The weight-regularization loss $\mathcal{L}_{\text{weights}}$ encourages the mixture weights of both heads to be close to one on transparent pixels (so $\sum_k \pi_k \approx 2$) and the two weights to sum to one on opaque pixels (so $\sum_k \pi_k \approx 1$). At inference, we use the weight sum to classify each pixel as transparent or opaque: when $\sum_k \pi_k > 1.5$, we treat the pixel as transparent and output both depth layers; otherwise we treat it as opaque and select a single depth via the component-selection rule of §3.3. This produces multi-layer depth on transparent pixels while preserving sharp boundaries on opaque ones. Full training and inference details are in §B.

4.2 Sky Estimation

Sky pixels have infinite depth, leading to extreme discontinuities at sky-scene boundaries and cause severe flying-point artifacts. Our representation can be extended to sky estimation by only adding an additional density component to account for the sky, leaving other components untouched.

Sky Component. The sky component has fixed mean μ_{sky} and scale b_{sky} , both set to large predefined constants and not updated during training. The resulting mixture is

$$p(D | \Theta) = \sum_{k=1}^K \pi_k \cdot \frac{1}{2b_k} \exp\left(-\frac{|\hat{D}_k - D|}{b_k}\right) + \pi_{K+1} \cdot \frac{1}{2b_{\text{sky}}} \exp\left(-\frac{|\mu_{\text{sky}} - D|}{b_{\text{sky}}}\right) \quad (5)$$

The finite-depth components continue to model scene geometry, while the sky component absorbs pixels whose depth should not be represented by a finite surface.

Table 2: Video Depth Evaluation. Our method stays on par with DA3 and VGGT and substantially outperforms PPD/PPVD.

Method	Type	Sintel		Bonn		KITTI	
		Abs Rel ↓	$\delta < 1.25$ ↑	Abs Rel ↓	$\delta < 1.25$ ↑	Abs Rel ↓	$\delta < 1.25$ ↑
PPD [31]	Diff	0.473	39.8	0.315	53.2	0.221	62.8
PPVD [32]	Diff	0.330	51.6	0.164	72.1	0.069	97.6
MoE3D [29]	FA	0.271	67.7	<u>0.053</u>	97.0	0.076	96.0
VGGT [24]	FA	0.297	68.8	<u>0.055</u>	97.1	0.073	96.5
DA3 [13]	FA	0.307	66.7	0.049	<u>97.2</u>	0.061	97.5
VGGT + Ours (GMM)	FA	<u>0.241</u>	<u>67.4</u>	0.076	94.2	<u>0.047</u>	98.0
DA3 + Ours (LMM)	FA	0.333	57.9	0.049	97.4	0.049	<u>97.9</u>
DA3 + Ours (GMM)	FA	0.223	67.0	<u>0.053</u>	<u>97.2</u>	0.044	<u>97.7</u>

Inference. We classify pixel i as sky if the sky component has the largest mixture weight:

$$\text{pixel } i \text{ is sky} \iff \pi_{K+1} = \max_{k \in \{1, \dots, K+1\}} \pi_k \quad (6)$$

This gives threshold-free sky segmentation from the mixture weights, requires no extra segmentation network, and prevents finite-depth components from creating flying points along the skyline.

5 Experiments

We organize the experiments into two parts: §5.1 evaluates our mixture-density representation on boundary and depth quality, and §5.2 evaluates the transparent-object and sky-region variants.

5.1 Boundary and Depth Quality

5.1.1 Experimental Settings

Implementation Details We instantiate the mixture head on DA3 [13] and VGGT [24] by replacing only the final DPT prediction layer. Unless stated otherwise, we use $K=4$ components, each predicting depth \hat{D}_k , confidence C_k^D , and mixture-weight π_k . We finetune the pretrained checkpoints on 4 RTX Pro 6000 GPUs for 10k steps, using a learning rate of $1e-4$ and a batch size of 48. Further details are provided in Appendix §B.

Training and Evaluation Datasets. Following DA3, we train on a mix of synthetic datasets: AriaSyntheticENV [16], HyperSim [20], MvsSynth [8], OmniWorld [37], PointOdyssey [36], TartanAir [27], vKitti2 [5], DynamicReplica [9], and UnrealStereo4K [35]. For evaluation, we use NRGBD [1], 7Scenes [22], and HiRoom [13] for boundary quality, and Sintel [4], Bonn [15], and KITTI [7] for video depth estimation.

Evaluation Metrics. For **boundary quality**, we follow exactly the same setting as Pixel-Perfect-Depth [31]: we extract edge masks from ground-truth depth maps with Canny operator and evaluate metrics on the masked point clouds. We report Chamfer Distance (CD↓) and Accuracy (Acc↓; mean predicted-to-GT distance) at two granularities: *per-image* (frame-level) and *per-sequence* (scene-level, aggregating point clouds across frames). We emphasize Acc because it is particularly sensitive to flying points: such points lie far from both foreground and background surfaces, resulting in large predicted-to-GT distances. For **inference speed**, we benchmark on a single L40S GPU at 504×384 resolution; the timing covers model inference and depth decoding. For **video depth estimation**, we follow the per-frame protocol of Cut3r [25] and Stream3r [11]: we report Absolute Relative error (AbsRel↓, the mean of $\frac{|\hat{D}-D|}{D}$) and threshold accuracy $\delta < 1.25$ (↑, the fraction of pixels with $\max\left(\frac{\hat{D}}{D}, \frac{D}{\hat{D}}\right) < 1.25$). Predictions are aligned to the ground truth before evaluation: a single global scale per sequence for DA3, VGGT, and Ours, and a per-frame scale and shift for PPD and PPVD.

5.1.2 Experimental Results

Boundary Quality. Table 1 shows that DA3+Ours achieves the lowest boundary CD and Acc across all datasets and granularities, often by a large margin. The gains are most visible in Acc, which

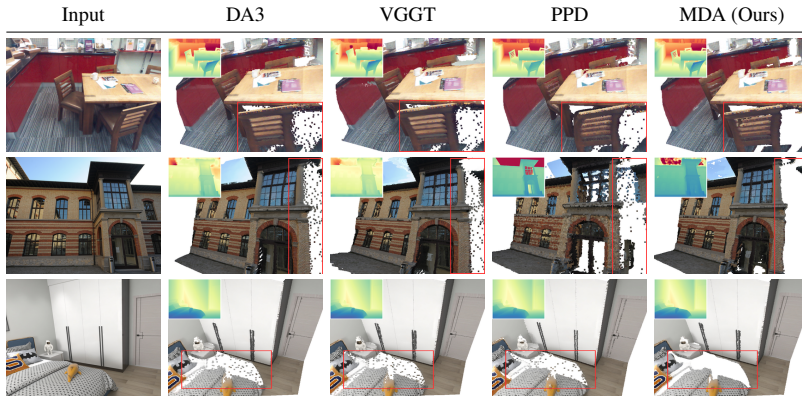


Figure 5: Qualitative boundary comparison. Baseline methods (DA3, VGGT, PPD) leave visible flying points on the boundaries, while our approach always keeps the boundary clean.

directly penalizes predicted points that fall away from both foreground and background surfaces. Figure 5 provides qualitative comparisons. All the baselines produce flying-point artifacts at object boundaries, while our predictions stay on foreground or background surfaces.

Inference Speed. The last column of Table 1 reports inference speed (FPS) of different methods. Our method adds negligible overhead: VGGT+Ours (34.11) and DA3+Ours (33.32) run at FPS comparable to their baselines (VGGT 33.43, DA3 36.78), since the only added computation is a lightweight $3K+1$ -channel output head. Diffusion-based methods (PPD, PPVD), in contrast, are roughly two orders of magnitude slower.

Video Depth Estimation. While we focus on improving boundary depth, our representation also preserves the standard reconstruction performance. To validate this, we evaluate the video depth quality and report the results in Table 2. DA3+Ours stays on par with DA3 across all three datasets, with clear gains on Sintel (AbsRel 0.223 vs. 0.307) and KITTI (0.044 vs. 0.061) and comparable performance on Bonn (0.053 vs. 0.049). VGGT+Ours similarly works slightly better than VGGT on most datasets. These results demonstrate the capability of preserving original depth estimation.

5.1.3 Experimental Analysis

Per-Component Analysis. We visualize each mixture component in Fig. 6. The components specialize spatially: each component dominates a different region of the scene. At boundaries, different components can account for the foreground or the background with a clean separation, reducing flying points. Additional scenes are provided in Appendix §C.1.3.

Robustness to Input Blur. Our mixture-density representation is especially useful when boundary evidence is weakened by blur. We simulate degraded inputs by downsampling each frame by factor s with area averaging and bicubic upsampling it back to the model resolution; larger s corresponds to stronger blur. We use the same evaluation protocol as above, and neither our model nor the baselines are trained with blur-specific augmentation. Figure 4 plots Acc and CD on NRGBD as a function of s , and Figure 7 provides qualitative results. As s increases, boundary locations become more ambiguous in the input. Unimodal baselines must still commit to a single depth per pixel, so their boundaries become progressively blurrier and accumulate more outliers. Our model degrades more gracefully because the mixture can keep foreground and background modes active even when the image evidence is weak.

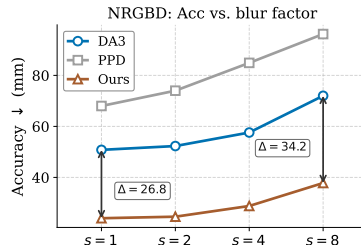


Figure 4: Boundary estimation Accuracy on NRGBD as a function of input blur s (Acc \downarrow , mm). Our mixture model degrades less compared to baselines.

Ablation: Representation vs. Architecture. Our mixture-density formulation changes both the network architecture (single \rightarrow multi-head) and the representation (unimodal \rightarrow mixture density).

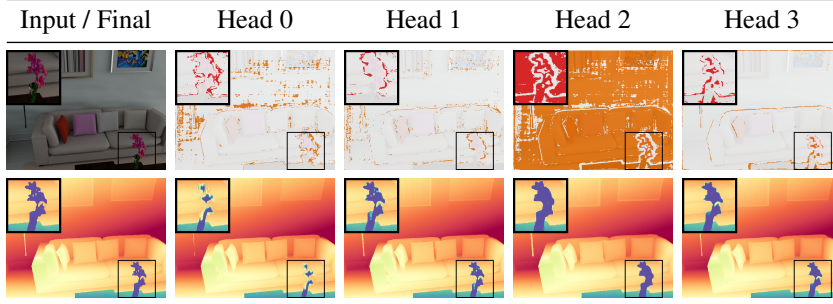


Figure 6: Per-component visualization with $K=4$ components. *Top*: the input image (leftmost) and the per-pixel mixture weight π_k for each head (brighter pixels indicate where head k wins the argmax). *Bottom*: our final fused depth (leftmost) and each head’s mean depth \hat{D}_k . The four heads specialize spatially: each head is dominant in a different region, and the boundaries between regions concentrate at occlusion edges.

Table 3: Ablation of representation and architecture. The largest gains come from replacing the unimodal depth representation with a mixture-density representation.

Method	NRGBD				HiRoom			
	Img		Seq		Img		Seq	
	Acc↓	CD↓	Acc↓	CD↓	Acc↓	CD↓	Acc↓	CD↓
Single-head + Unimodal ℓ_1 (DA3)	57.0	50.0	51.0	43.5	42.0	40.0	38.0	32.0
Single-head + Unimodal ℓ_1 (Finetuned DA3)	54.0	49.0	48.0	42.5	38.0	36.0	35.0	30.0
Multi-head + Unimodal ℓ_1	50.0	46.5	44.0	40.0	39.0	36.5	36.0	30.5
Multi-head + Unimodal ℓ_2 + entropy	56.0	49.0	49.5	45.0	46.5	46.0	44.0	37.0
Multi-head + Mixture-density ℓ_1 (Ours)	25.0	35.5	22.0	29.5	31.0	34.5	29.0	28.0

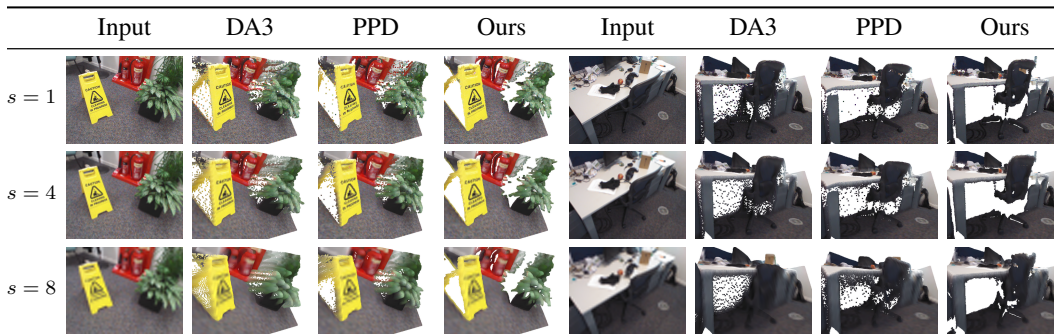
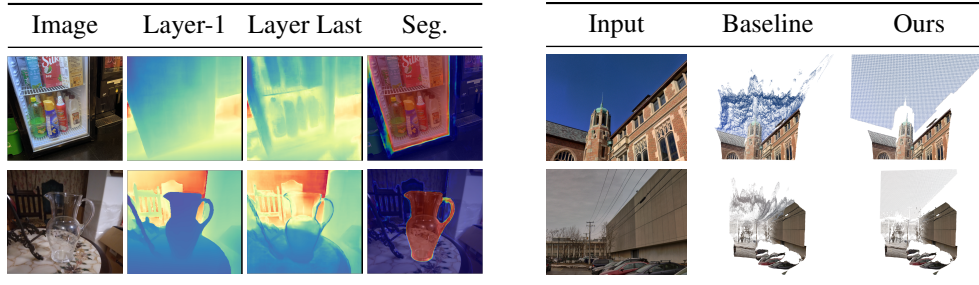


Figure 7: Qualitative boundary reconstruction under input blur. As s increases, baselines (DA3, PPD) accumulate thick bands of flying points at boundaries, while our model preserves clean boundary separation throughout.

To isolate their effects, Table 3 ablates the two design choices on the DA3 backbone. We also include a multi-head baseline with ℓ_2 loss and entropy regularization, following MoE3D, which is intended as a controlled architectural comparison rather than a reproduction of MoE3D. Except for the first row (the original DA3), all variants are trained with the same data and optimization setting. Finetuning and multi-head architecture bring modest gains, while replacing the unimodal representation with a mixture density accounts for most of the boundary improvement. This indicates that the representation, rather than the extra heads alone, is the main driver of performance.

5.2 Experiments on Extensions

Transparent Object Depth. We evaluate multi-layer depth estimation on the LayeredDepth benchmark [30], which provides a synthetic validation set and a real-world validation set with human annotations; full quantitative results are deferred to §C.2.1. For transparent objects, our sigmoid-weighted mixture formulation (§4.1) recovers both the visible transparent surface and the occluded background behind it. Figure 8a shows multi-layer predictions on real LayeredDepth scenes: despite training only on synthetic supervision, the mixture head produces a clean first-layer depth aligned with the visible transparent surface and a plausible last-layer depth behind it.



(a) Our multi-layer depth prediction on transparent objects: input image, predicted first depth layer (visible transparent surface), predicted last depth layer (occluded geometry behind it), and transparency segmentation.

(b) Sky comparison: input image, baseline trained without the sky component (flying points along the entire skyline), and our model with the sky component (clean sky boundaries).

Figure 8: Qualitative results on transparent objects and sky.

Sky Estimation. To validate the dedicated sky component, we evaluate sky-segmentation quality on Sintel, reporting IoU against its semantic-segmentation ground truth; full quantitative results are deferred to §C.2.2. Figure 8b shows qualitative comparisons against a baseline identical to ours except for the missing sky component. Without the sky component, the baseline must place every sky pixel at a finite depth, producing flying points along the entire skyline. In contrast, our model assigns sky pixels to the sky component, producing clean sky boundaries.

6 Conclusion

We presented a mixture-density formulation that removes *flying points* at object boundaries by replacing the unimodal NLL with a mixture NLL over K components — a final-layer modification that leaves the backbone, input resolution, and inference budget untouched. Instantiated on DA3 and VGGT, it substantially reduces boundary error over every baseline at $\sim 80\times$ the speed of diffusion-based approaches, and extends naturally to transparent surfaces and sky within the same head.

Acknowledgments

We thank Siyi Chen, Zhaoning Wang, and Yi Zhong for fruitful discussions, Zichen Wang for insightful conversations and inspiration from his MoE3D [29] work, and Gangwei Xu for help in running PPD [31] and PPVD [32].

References

- [1] Dejan Azinović, Ricardo Martin-Brualla, Dan B. Goldman, Matthias Nießner, and Justus Thies. Neural RGB-D surface reconstruction. In *Proceedings of the IEEE/CVF Conference on Computer Vision and Pattern Recognition*, 2022.
- [2] Yoshua Bengio, Nicholas Léonard, and Aaron Courville. Estimating or propagating gradients through stochastic neurons for conditional computation. *arXiv preprint arXiv:1308.3432*, 2013.
- [3] Pierre Blanchard, Desmond J Higham, and Nicholas J Higham. Accurately computing the log-sum-exp and softmax functions. *IMA Journal of Numerical Analysis*, 41(4):2311–2330, 2021.
- [4] Daniel J. Butler, Jonas Wulff, Garrett B. Stanley, and Michael J. Black. A naturalistic open source movie for optical flow evaluation. In *European Conference on Computer Vision*, 2012.
- [5] Yohann Cabon, Naila Murray, and Martin Humenberger. Virtual KITTI 2. *arXiv preprint arXiv:2001.10773*, 2020.
- [6] David Eigen, Christian Puhrsch, and Rob Fergus. Depth map prediction from a single image using a multi-scale deep network. *Advances in neural information processing systems*, 27, 2014.
- [7] Andreas Geiger, Philip Lenz, Christoph Stiller, and Raquel Urtasun. Vision meets robotics: The KITTI dataset. *International Journal of Robotics Research (IJRR)*, 32(11):1231–1237, 2013.

- [8] Po-Han Huang, Kevin Matzen, Johannes Kopf, Narendra Ahuja, and Jia-Bin Huang. DeepMVS: Learning multi-view stereopsis. In *Proceedings of the IEEE/CVF Conference on Computer Vision and Pattern Recognition*, 2018.
- [9] Nikita Karaev, Ignacio Rocco, Benjamin Graham, Natalia Neverova, Andrea Vedaldi, and Christian Rupprecht. DynamicStereo: Consistent dynamic depth from stereo videos. In *Proceedings of the IEEE/CVF Conference on Computer Vision and Pattern Recognition*, 2023.
- [10] Nikhil Keetha, Norman Müller, Johannes Schönberger, Lorenzo Porzi, Yuchen Zhang, Tobias Fischer, Arno Knapitsch, Duncan Zauss, Ethan Weber, Nelson Antunes, et al. Mapanything: Universal feed-forward metric 3d reconstruction. *arXiv preprint arXiv:2509.13414*, 2025.
- [11] Yushi Lan, Yihang Luo, Fangzhou Hong, Shangchen Zhou, Honghua Chen, Zhaoyang Lyu, Shuai Yang, Bo Dai, Chen Change Loy, and Xingang Pan. Stream3r: Scalable sequential 3d reconstruction with causal transformer. *arXiv preprint arXiv:2508.10893*, 2025.
- [12] Vincent Leroy, Yohann Cabon, and Jérôme Revaud. Grounding image matching in 3d with mast3r. In *European conference on computer vision*, pages 71–91. Springer, 2024.
- [13] Haotong Lin, Sili Chen, Jun Hao Liew, Donny Y. Chen, Zhenyu Li, Guang Shi, Jiashi Feng, and Bingyi Kang. Depth anything 3: Recovering the visual space from any views. *arXiv preprint arXiv:2511.10647*, 2025.
- [14] Lu Ling, Yichen Sheng, Zhi Tu, Wentian Zhao, Cheng Xin, Kun Wan, Lantao Yu, Qianyu Guo, Zixun Yu, Yawen Lu, et al. D13dv-10k: A large-scale scene dataset for deep learning-based 3d vision. In *Proceedings of the IEEE/CVF Conference on Computer Vision and Pattern Recognition*, pages 22160–22169, 2024.
- [15] Emanuele Palazzolo, Jens Behley, Philipp Lottes, Philippe Giguère, and Cyrill Stachniss. ReFusion: 3d reconstruction in dynamic environments for RGB-D cameras exploiting residuals. In *IEEE/RSJ International Conference on Intelligent Robots and Systems (IROS)*, 2019.
- [16] Xiaqing Pan, Nicholas Charron, Yongqian Yang, Scott Peters, Thomas Whelan, Chen Kong, Omkar Parkhi, Richard Newcombe, and Yuheng Carl Ren. Aria digital twin: A new benchmark dataset for egocentric 3d machine perception. In *Proceedings of the IEEE/CVF International Conference on Computer Vision*, pages 20133–20143, 2023.
- [17] Pierluigi Zama Ramirez, Fabio Tosi, Matteo Poggi, Samuele Salti, Stefano Mattoccia, and Luigi Di Stefano. Open challenges in deep stereo: the booster dataset. In *Proceedings of the IEEE/CVF Conference on Computer Vision and Pattern Recognition*, pages 21168–21178, 2022.
- [18] René Ranftl, Katrin Lasinger, David Hafner, Konrad Schindler, and Vladlen Koltun. Towards robust monocular depth estimation: Mixing datasets for zero-shot cross-dataset transfer. *IEEE transactions on pattern analysis and machine intelligence*, 44(3):1623–1637, 2020.
- [19] René Ranftl, Alexey Bochkovskiy, and Vladlen Koltun. Vision transformers for dense prediction. In *Proceedings of the IEEE/CVF international conference on computer vision*, pages 12179–12188, 2021.
- [20] Mike Roberts, Jason Ramapuram, Anurag Ranjan, Atulit Kumar, Miguel Angel Bautista, Nathan Paczan, Russ Webb, and Joshua M Susskind. Hypersim: A photorealistic synthetic dataset for holistic indoor scene understanding. In *Proceedings of the IEEE/CVF international conference on computer vision*, pages 10912–10922, 2021.
- [21] Shreeyak Sajjan, Matthew Moore, Mike Pan, Ganesh Nagaraja, Johnny Lee, Andy Zeng, and Shuran Song. Clear grasp: 3d shape estimation of transparent objects for manipulation. In *2020 IEEE international conference on robotics and automation (ICRA)*, pages 3634–3642. IEEE, 2020.
- [22] Jamie Shotton, Ben Glocker, Christopher Zach, Shahram Izadi, Antonio Criminisi, and Andrew Fitzgibbon. Scene coordinate regression forests for camera relocalization in RGB-D images. In *Proceedings of the IEEE/CVF Conference on Computer Vision and Pattern Recognition*, 2013.

- [23] Fabio Tosi, Yiyi Liao, Carolin Schmitt, and Andreas Geiger. Smd-nets: Stereo mixture density networks. In *Proceedings of the IEEE/CVF conference on computer vision and pattern recognition*, pages 8942–8952, 2021.
- [24] Jianyuan Wang, Minghao Chen, Nikita Karaev, Andrea Vedaldi, Christian Rupprecht, and David Novotny. Vggt: Visual geometry grounded transformer. In *Proceedings of the IEEE/CVF Conference on Computer Vision and Pattern Recognition*, 2025.
- [25] Qianqian Wang, Yifei Zhang, Aleksander Holynski, Alexei A Efros, and Angjoo Kanazawa. Continuous 3d perception model with persistent state. pages 10510–10522, 2025.
- [26] Shuzhe Wang, Vincent Leroy, Yohann Cabon, Boris Chidlovskii, and Jerome Revaud. Dust3r: Geometric 3d vision made easy. In *Proceedings of the IEEE/CVF conference on computer vision and pattern recognition*, pages 20697–20709, 2024.
- [27] Wenshan Wang, Delong Zhu, Xiangwei Wang, Yaoyu Hu, Yuheng Qiu, Chen Wang, Yafei Hu, Ashish Kapoor, and Sebastian Scherer. Tartanair: A dataset to push the limits of visual slam. In *2020 IEEE/RSJ International Conference on Intelligent Robots and Systems (IROS)*, pages 4909–4916. IEEE, 2020.
- [28] Yifan Wang, Jianjun Zhou, Haoyi Zhu, Wenzheng Chang, Yang Zhou, Zizun Li, Junyi Chen, Jiangmiao Pang, Chunhua Shen, and Tong He. π^3 : Permutation-equivariant visual geometry learning. *arXiv preprint arXiv:2507.13347*, 2025.
- [29] Zichen Wang, Ang Cao, Liam J. Wang, and Jeong Joon Park. MoE3D: A mixture-of-experts module for 3D reconstruction. *arXiv preprint arXiv:2601.05208*, 2026.
- [30] Hongyu Wen, Yiming Zuo, Venkat Subramanian, Patrick Chen, and Jia Deng. Seeing and seeing through the glass: Real and synthetic data for multi-layer depth estimation. pages 6715–6725, 2025.
- [31] Gangwei Xu, Haotong Lin, Hongcheng Luo, Xianqi Wang, Jingfeng Yao, Lianghui Zhu, Yuechuan Pu, Cheng Chi, Haiyang Sun, Bing Wang, et al. Pixel-perfect depth with semantics-prompted diffusion transformers. *arXiv preprint arXiv:2510.07316*, 2025.
- [32] Gangwei Xu, Haotong Lin, Hongcheng Luo, Haiyang Sun, Bing Wang, Guang Chen, Sida Peng, Hangjun Ye, and Xin Yang. Pixel-perfect visual geometry estimation. *arXiv preprint arXiv:2601.05246*, 2026.
- [33] Lihe Yang, Bingyi Kang, Zilong Huang, Xiaogang Xu, Jiashi Feng, and Hengshuang Zhao. Depth anything: Unleashing the power of large-scale unlabeled data. In *Proceedings of the IEEE/CVF conference on computer vision and pattern recognition*, pages 10371–10381, 2024.
- [34] Lihe Yang, Bingyi Kang, Zilong Huang, Zhen Zhao, Xiaogang Xu, Jiashi Feng, and Hengshuang Zhao. Depth anything v2. volume 37, pages 21875–21911, 2024.
- [35] Yi Zhang, Weichao Qiu, Qi Chen, Xiaolin Hu, and Alan Yuille. UnrealStereo: Controlling hazardous factors to analyze stereo vision. In *International Conference on 3D Vision (3DV)*, 2018.
- [36] Yang Zheng, Adam W. Harley, Bokui Shen, Gordon Wetzstein, and Leonidas J. Guibas. PointOdyssey: A large-scale synthetic dataset for long-term point tracking. In *Proceedings of the IEEE/CVF International Conference on Computer Vision*, 2023.
- [37] Yang Zhou, Yifan Wang, Jianjun Zhou, Wenzheng Chang, Haoyu Guo, Zizun Li, Kaijing Ma, Xinyue Li, Yating Wang, Haoyi Zhu, et al. Omniworld: A multi-domain and multi-modal dataset for 4d world modeling. *arXiv preprint arXiv:2509.12201*, 2025.

Supplementary Material

Modeling Depth Ambiguity: A Mixture-Density Representation for Flying-Point-Free Depth Estimation

This supplementary material is organized as below. §A provides the full derivations deferred from the main paper: including the complete Laplacian and Gaussian mixture derivation, the log-depth parameterization used at training, and a gradient analysis showing why the mixture representation is robust at depth boundaries. §B describes the architecture, training objective, and optimization for both the boundary-handling model and the transparent-object variant. §C reports additional experiments: boundary and depth quality (§C.1, including multi-view reconstruction, ablations on the number of components, and the inference rule, and extra qualitative results) and the two extensions (§C.2, including additional transparent-object and sky-component results). Finally, §D discusses failure cases and limitations of our method.

A Method Details

This section expands the derivations that were abbreviated in the main paper. We first show why the standard confidence-weighted ℓ_1 loss is a unimodal Laplacian NLL, then derive the Laplacian mixture loss (Eq. 3). We then present the unimodal and mixture Gaussian variants in one place (§3.1 and §3.4) and close with the log-depth parameterization used for the Gaussian variant.

A.1 Full Derivation of the Laplacian Mixture Representation

Unimodal Laplacian. For a single pixel i , the unimodal Laplacian model from §3.1 places a Laplace distribution centered at the predicted depth \hat{D} with scale b :

$$p(D | \hat{D}, b) = \frac{1}{2b} \exp\left(-\frac{|D - \hat{D}|}{b}\right). \quad (7)$$

Assuming pixels are independent, the negative log-likelihood over all N pixels is:

$$\mathcal{L}_{\text{Uni}} = \sum_{i=1}^N \left(\frac{|\hat{D} - D|}{b} + \log b + \log 2 \right). \quad (8)$$

Using the confidence reparameterization $C^D = \alpha/b$, we have $b = \alpha/C^D$ and therefore:

$$\begin{aligned} \mathcal{L}_{\text{Uni}} &= \frac{1}{\alpha} \sum_{i=1}^N \left(C^D |\hat{D} - D| - \alpha \log C^D + \alpha \log(2\alpha) \right) \\ &= \frac{1}{\alpha} \mathcal{L}_{\text{Depth}} + N \log(2\alpha). \end{aligned} \quad (9)$$

Thus minimizing the confidence-weighted ℓ_1 loss in Eq. 1 is equivalent to minimizing the NLL of a unimodal Laplacian depth distribution, up to a positive scale and an additive constant.

Laplacian Mixture. The Laplacian mixture (§3.2, Eq. 2) replaces this single component with a convex combination of K Laplacian densities:

$$p(D | \{\hat{D}_k, b_k, \pi_k\}_{k=1}^K) = \sum_{k=1}^K \pi_k \cdot \frac{1}{2b_k} \exp\left(-\frac{|D - \hat{D}_k|}{b_k}\right), \quad (10)$$

with mixture weights $\pi_k \in [0, 1]$ satisfying $\sum_{k=1}^K \pi_k = 1$ and per-component scales $b_k > 0$. Each component represents one depth hypothesis weighted by its mixing probability.

Loss Derivation. We provide the full derivation of the Laplacian mixture loss (Eq. 3 in the main paper). Starting from the negative log of the mixture density above and applying the confidence reparameterization $C_k^D = \alpha/b_k$, the log-likelihood of a single Laplace component k becomes:

$$\log \frac{1}{2b_k} \exp\left(-\frac{|\hat{D}_k - D|}{b_k}\right) = -\frac{1}{\alpha} \left(C_k^D |\hat{D}_k - D| - \alpha \log C_k^D \right) - \log(2\alpha). \quad (11)$$

The term inside the parentheses is exactly the per-component version of the unimodal Laplacian loss from Eq. 1, now applied to each mixture component independently.

Let $\mathcal{L}_k^{\text{Laplace}} = C_k^D |\hat{D}_k - D| - \alpha \log C_k^D$ denote this per-component loss. Substituting back into the mixture NLL, the argument of the outer log becomes:

$$\sum_{k=1}^K \pi_k \cdot \frac{1}{2b_k} \exp\left(-\frac{|\hat{D}_k - D|}{b_k}\right) = \frac{1}{2\alpha} \sum_{k=1}^K \exp\left(\log \pi_k - \frac{1}{\alpha} \mathcal{L}_k^{\text{Laplace}}\right). \quad (12)$$

Taking the negative log and dropping the constant $\log(2\alpha)$ yields the final loss (Eq. 3):

$$\mathcal{L}_{\text{Mix}} = -\sum_{i=1}^N \log \sum_{k=1}^K \exp\left(\log \pi_k - \frac{1}{\alpha} \mathcal{L}_k^{\text{Laplace}}\right). \quad (13)$$

LogSumExp Stabilization. Direct evaluation of $\log \sum_k \exp(a_k)$ is numerically unstable when any a_k is large. We stabilize it with the LogSumExp trick [3]. Defining $a_k = \log \pi_k - \frac{1}{\alpha} \mathcal{L}_k^{\text{Laplace}}$ and $a^* = \max_k a_k$:

$$\log \sum_k e^{a_k} = a^* + \log \sum_k e^{a_k - a^*}, \quad (14)$$

where all terms $a_k - a^* \leq 0$, so the exponentials never overflow.

A.2 Full Derivation of the Gaussian Mixture Representation

Unimodal Gaussian. For a single pixel i , the unimodal Gaussian model places a Gaussian distribution centered at the predicted depth \hat{D} with variance σ^2 :

$$p(D | \hat{D}, \sigma^2) = \frac{1}{\sqrt{2\pi\sigma^2}} \exp\left(-\frac{\|\hat{D} - D\|^2}{2\sigma^2}\right). \quad (15)$$

Assuming pixels are independent, the negative log-likelihood over all N pixels is:

$$\mathcal{L}_{\text{NLL}} = \sum_{i=1}^N \left(\frac{\|\hat{D} - D\|^2}{2\sigma^2} + \frac{1}{2} \log \sigma^2 + \frac{1}{2} \log(2\pi) \right). \quad (16)$$

Using the confidence reparameterization $C^D = \alpha/\sigma^2$, we have $\sigma^2 = \alpha/C^D$ and therefore:

$$\begin{aligned} \mathcal{L}_{\text{NLL}} &= \frac{1}{2\alpha} \sum_{i=1}^N \left(C^D \|\hat{D} - D\|^2 - \alpha \log C^D + \alpha \log(2\pi\alpha) \right) \\ &= \frac{1}{2\alpha} \mathcal{L}_{\text{Gaussian}} + \frac{N}{2} \log(2\pi\alpha), \end{aligned} \quad (17)$$

where $\mathcal{L}_{\text{Gaussian}} = \sum_{i=1}^N \left(C^D \|\hat{D} - D\|^2 - \alpha \log C^D \right)$ is the confidence-weighted ℓ_2 loss. Compared with Eq. 1, the Gaussian formulation replaces the absolute error with the squared error but retains the same confidence-weighted data-fidelity plus log-barrier structure.

Gaussian Mixture. The Gaussian mixture (§3.4) replaces this single component with a convex combination of K Gaussian densities:

$$p(D | \{\hat{D}_k, \sigma_k^2, \pi_k\}_{k=1}^K) = \sum_{k=1}^K \pi_k \cdot \frac{1}{\sqrt{2\pi\sigma_k^2}} \exp\left(-\frac{\|\hat{D}_k - D\|^2}{2\sigma_k^2}\right), \quad (18)$$

with mixture weights $\pi_k \in [0, 1]$ satisfying $\sum_{k=1}^K \pi_k = 1$ and per-component variances $\sigma_k^2 > 0$. As in the Laplacian mixture, each component represents one depth hypothesis; the Gaussian assumption changes the component shape from an ℓ_1 -based density to an ℓ_2 -based density.

Loss Derivation. Starting from the negative log of the Gaussian mixture density and applying the confidence reparameterization $C_k^D = \alpha/\sigma_k^2$, the log-likelihood of a single Gaussian component k becomes:

$$\log \frac{1}{\sqrt{2\pi\sigma_k^2}} \exp\left(-\frac{\|\hat{D}_k - D\|^2}{2\sigma_k^2}\right) = -\frac{1}{2\alpha} \left(C_k^D \|\hat{D}_k - D\|^2 - \alpha \log C_k^D\right) - \frac{1}{2} \log(2\pi\alpha). \quad (19)$$

Let $\mathcal{L}_k^{\text{Gaussian}} = C_k^D \|\hat{D}_k - D\|^2 - \alpha \log C_k^D$ denote the per-component Gaussian loss. Substituting back into the mixture NLL, the argument of the outer log becomes:

$$\sum_{k=1}^K \pi_k \cdot \frac{1}{\sqrt{2\pi\sigma_k^2}} \exp\left(-\frac{\|\hat{D}_k - D\|^2}{2\sigma_k^2}\right) = \frac{1}{\sqrt{2\pi\alpha}} \sum_{k=1}^K \exp\left(\log \pi_k - \frac{1}{2\alpha} \mathcal{L}_k^{\text{Gaussian}}\right). \quad (20)$$

Taking the negative log and dropping the constant $\frac{1}{2} \log(2\pi\alpha)$ yields the final loss:

$$\mathcal{L}_{\text{GMM}} = -\sum_{i=1}^N \log \sum_{k=1}^K \exp\left(\log \pi_k - \frac{1}{2\alpha} \mathcal{L}_k^{\text{Gaussian}}\right). \quad (21)$$

The only differences from the Laplacian mixture loss \mathcal{L}_{Mix} are the squared error in $\mathcal{L}_k^{\text{Gaussian}}$ and the factor $1/(2\alpha)$ in the exponent, instead of $1/\alpha$ for the Laplacian case.

LogSumExp Stabilization. Defining $a_k = \log \pi_k - \frac{1}{2\alpha} \mathcal{L}_k^{\text{Gaussian}}$ and $a^* = \max_k a_k$, the same LogSumExp identity from §A.1 gives $\log \sum_k e^{a_k} = a^* + \log \sum_k e^{a_k - a^*}$, with all exponents non-positive and therefore numerically safe.

A.3 Log-Depth Parameterization for Gaussian Mixture

Raw depth values span a very large dynamic range across scenes (from centimeters at near-field objects to tens of meters outdoors), which makes a Gaussian likelihood in linear depth poorly calibrated: the ℓ_2 penalty disproportionately magnifies errors at far distances. Following [31, 10], we therefore apply the Gaussian mixture in log-depth space.

Concretely, every component mean \hat{D}_k , variance σ_k^2 , and the ground-truth target are mapped through $f(D) = \log(D+\epsilon)$ before the loss is evaluated, where ϵ is a small constant (0.1 in our implementation) that prevents numerical instability for near-zero depth values. A Gaussian in log-space corresponds to a log-normal in linear space, which better matches the heavy-tailed distribution of scene depth. The inverse map $D = \exp(f) - \epsilon$ is applied at inference to recover linear depth. The Laplacian mixture uses the original depth space, since its ℓ_1 penalty is already robust to the heavy-tailed depth distribution and does not benefit from log-space reparameterization in our experiments.

A.4 Gradient Analysis: Why the Mixture-Density Representation Is Robust at Boundaries

This section explains the boundary robustness of our mixture representation from a **gradient perspective**. At ambiguous boundary pixels, some training labels may correspond to the foreground surface and others to the background surface, even when the local image evidence is similar. We show that the mixture NLL tolerates this ambiguity without dragging depth components into the empty space between foreground and background surfaces, thus avoiding flying points.

This robustness follows from the gradient structure of the mixture NLL: each component’s update is gated by its posterior responsibility, so a component that already fits the foreground receives almost no depth gradient from a background label, and vice versa (Fig. 6). A unimodal head has no such mechanism. Inconsistent boundary labels instead pull the single prediction across the depth discontinuity, causing it to settle at an averaged depth between surfaces and produce a flying point. We give the derivation for the Laplacian mixture (LMM); the Gaussian mixture has the same form.

Setup. Consider a single pixel with ground-truth depth D and predicted Laplacian mixture

$$p(D) = \sum_{k=1}^K \pi_k \cdot \frac{1}{2b_k} \exp\left(-\frac{|D - \hat{D}_k|}{b_k}\right), \quad \pi_k = \frac{\exp(\pi'_k)}{\sum_{j=1}^K \exp(\pi'_j)}, \quad (22)$$

where mixture weights π_k come from a softmax over per-component logits π'_k . The per-pixel NLL is $\mathcal{L} := -\log p(D)$. We define the *posterior responsibility* of component k as

$$\gamma_k := \frac{\pi_k \frac{1}{2b_k} \exp(-|D - \hat{D}_k|/b_k)}{p(D)}, \quad \sum_{k=1}^K \gamma_k = 1, \quad (23)$$

i.e. the posterior probability that component k explains the observed depth D under the current mixture parameters.

Gradients are Gated by γ_k . For any parameter θ_k of component k (i.e. \hat{D}_k or b_k), differentiating \mathcal{L} and using Eq. 23 gives

$$\frac{\partial \mathcal{L}}{\partial \theta_k} = -\gamma_k \cdot \frac{\partial \log p_k(D)}{\partial \theta_k}, \quad \log p_k(D) = -\log(2b_k) - \frac{|D - \hat{D}_k|}{b_k}. \quad (24)$$

The mixture gradient on each component is exactly the single-Laplacian gradient on that component, scaled by the responsibility γ_k . In particular, for the depth prediction \hat{D}_k we obtain

$$\frac{\partial \mathcal{L}}{\partial \hat{D}_k} = -\gamma_k \frac{\text{sgn}(D - \hat{D}_k)}{b_k}. \quad (25)$$

Boundary-Robustness Consequence. Consider the two-component case ($K=2$) at a converged boundary pixel. Suppose component 1 has captured the foreground surface ($\hat{D}_1 \approx d_{\text{fg}}$) and component 2 has captured the background surface ($\hat{D}_2 \approx d_{\text{bg}}$), with $|d_{\text{fg}} - d_{\text{bg}}| \gg b_1, b_2$. If the ground-truth label at this pixel falls on the foreground ($D \approx d_{\text{fg}}$), the density ratio in Eq. 23 becomes

$$\frac{p_1(D)}{p_2(D)} = \frac{b_2}{b_1} \exp\left(\frac{|D - d_{\text{bg}}|}{b_2} - \frac{|D - d_{\text{fg}}|}{b_1}\right),$$

which is exponentially large because $|D - d_{\text{fg}}| \approx 0$ while $|D - d_{\text{bg}}| \approx |d_{\text{fg}} - d_{\text{bg}}| \gg b_2$. Hence $\gamma_1 \approx 1$ and $\gamma_2 \approx 0$. Substituting $\gamma_2 \approx 0$ into Eq. 25 gives $\partial \mathcal{L} / \partial \hat{D}_2 \approx 0$: *the background component receives essentially no depth gradient*, so the mis-assigned label cannot drag \hat{D}_2 off the background surface and no flying point arises. The mixing-logit gradients $\partial \mathcal{L} / \partial \pi'_k = \pi_k - \gamma_k$ shift weight from π_2 toward π_1 , while the depth values \hat{D}_1, \hat{D}_2 stay locked to their respective surfaces.

Comparison to a Unimodal Head. A unimodal Laplacian head has no such gating mechanism: with a single prediction \hat{D} and scale b , the gradient on the depth value is $\partial \mathcal{L} / \partial \hat{D} = -\text{sgn}(D - \hat{D})/b$, which is always non-zero and points toward the depth label. If the network predicts $\hat{D} \approx d_{\text{bg}}$ but the label lies on the foreground surface $D = d_{\text{fg}}$, the gradient drags \hat{D} from the background surface toward the foreground surface. The reverse happens for background labels. Accumulated over many ambiguous boundary pixels, these opposing pulls drive the single prediction toward a compromise between surfaces, producing a flying point.

A Common Misunderstanding: Multi-Depth Supervision Is Not Required. There might be a misunderstanding that training a multi-depth representation requires multi-depth ground truth, e.g., one annotated depth per surface at boundary pixels. This is not the case. Although each training pixel carries only a single depth label, boundary pixels with similar local image evidence can receive *different* labels depending on subpixel foreground/background coverage. Under a unimodal loss these inconsistent labels induce averaging, since a single prediction must minimize the loss against all of them simultaneously. Under our mixture likelihood, different components instead explain different subsets of these labels through their posterior responsibilities γ_k (Eq. 23), as the gradient analysis above shows. The mixture therefore acquires multi-surface specialization from ordinary single-depth supervision, without any multi-layer or per-surface annotations.

B Extra Implementation Details

B.1 Model Architecture

Our mixture head is backbone-agnostic: it only modifies the output projection of the underlying depth predictor, so it can be applied to most modern depth estimators [13, 24] with no other architectural

change. For each of the K components, the head emits three per-pixel quantities: (i) a depth prediction \hat{D}_k , (ii) a confidence $C_k^D = \alpha/b_k$, and (iii) a mixture-weight logit, normalized via softmax over the K components to produce π_k . The head therefore adds $3K$ scalar outputs per pixel on top of whatever the backbone already produces. We instantiate it on top of DA3 and VGGT by replacing the final layer of the DPT head with this projection, using $K=4$ components by default.

B.2 Implementation Details for Boundary Handling Model

Probability Clamp for Preventing Component Collapse. A key practical challenge is component collapse: the network may assign a near-one mixture weight π_k to one component and near-zero weights to the others, effectively reducing the mixture to a unimodal predictor. We prevent this with a probability clamp. During the forward pass, each mixture weight is clipped to a minimum value π_{\min} and renormalized,

$$\tilde{\pi}'_k = \max(\pi_k, \pi_{\min}), \quad \hat{\pi}_k = \frac{\tilde{\pi}'_k}{\sum_j \tilde{\pi}'_{i,j}}, \quad (26)$$

and the clamped weights $\hat{\pi}_k$ enter the mixture NLL (Eq. 3) so every component receives a non-negligible gradient on its depth and scale predictions. In the backward pass we apply the straight-through estimator [2]: gradients flow through the clamp as if it were the identity, so the original (unclamped) logits are still updated normally and can learn to distribute probability mass freely. This prevents collapse without distorting the gradient landscape.

Training Objective. The full training objective combines the mixture depth loss (Eq. 3) with a camera pose loss and point cloud loss inherited from DA3. For camera pose, we use the output of DA3’s lightweight camera head rather than the camera-ray prediction from the Dual-DPT head, both during training and at inference. The camera pose loss is:

$$\mathcal{L}_{\text{pose}} = \sum_{t=1}^N \left(\|\hat{\mathbf{q}}_t - \mathbf{q}_t\|_2 + \left\| \frac{\hat{\boldsymbol{\tau}}_t}{\hat{s}} - \frac{\boldsymbol{\tau}_t}{s} \right\|_2 + \|\hat{\mathbf{f}}_t - \mathbf{f}_t\|_2 \right), \quad (27)$$

where \mathbf{q}_t , $\boldsymbol{\tau}_t$, and \mathbf{f}_t denote the per-frame rotation quaternion, translation, and focal length, and s , \hat{s} are the ground-truth and predicted global scale factors calculated similar to [28].

Initialization, Curriculum, and Optimization. We instantiate the mixture head on the multiview depth estimator DA3-GIANT [13] and VGGT [24], and initialize from the corresponding pretrained checkpoint. Because our mixture head replicates the original final prediction layer into K parallel branches, all K copies start with identical weights. To break the symmetry between mixture heads, we add zero-mean Gaussian noise to each duplicated weight tensor, with standard deviation $0.1 \cdot \text{mean}(|w|)$ where w is the corresponding original weight.

Training proceeds in three stages, each using the same optimizer (learning rate $1e-4$, effective batch size 48 via gradient accumulation, on 4 RTX Pro 6000 GPUs), for a total of 11,000 steps: (i) we freeze the backbone and all DPT-head layers except the new mixture projection and train only the mixture-head weights for 1,000 steps; (ii) we unfreeze the remaining DPT-head layers — the backbone is still frozen — and train for another 5,000 steps; and (iii) we additionally unfreeze the local-attention layers of the backbone and train for 5,000 steps. This curriculum stabilizes the early phase of training and preserves the backbone’s pretrained capacity, letting us match the underlying model’s depth quality with substantially less training data and compute. Following DA3, the base resolution is 504×504 and training image resolutions are randomly sampled from $\{504 \times 504, 504 \times 378, 504 \times 336, 504 \times 280, 504 \times 210, 504 \times 154, 378 \times 504, 336 \times 504, 280 \times 504, 672 \times 504\}$, while the number of views is sampled uniformly from $[2, 24]$.

B.3 Implementation Details for Transparent Object Variant

Training Objective. For the transparent-object variant of §4.1, we use $K=2$ depth heads, with the first supervised on the visible (front) surface and the second on the occluded (back) surface for transparent pixels. The full per-pixel training loss combines a transparency-aware depth loss with a weight-regularization term:

$$\mathcal{L}_{\text{trans}} = \mathcal{L}_{\text{depth}} + \mathcal{L}_{\text{weights}}. \quad (28)$$

Depth loss. On opaque pixels, only one surface is visible and we keep the mixture NLL from the main paper (Eq. 3); the two heads remain free to maintain different depth hypotheses, retaining the boundary handling of the main model. On transparent pixels, both layers are visible and we instead supervise each head independently on its assigned ground-truth layer with a single-component Laplacian NLL:

$$\mathcal{L}_{\text{depth}} = \begin{cases} \mathcal{L}_1^{\text{Lap}}(D^{(1)}) + \mathcal{L}_2^{\text{Lap}}(D^{(L)}), & \text{if pixel is transparent,} \\ \mathcal{L}_{\text{mix}}(D), & \text{otherwise (opaque),} \end{cases} \quad (29)$$

where $D^{(1)}$ and $D^{(L)}$ are the first-layer (visible) and last-layer (occluded) ground-truth depths from LayeredDepth, $\mathcal{L}_k^{\text{Lap}}(g)$ is the single-component Laplacian NLL of §3.1 (Eq. 1) applied to head k with label g , and $\mathcal{L}_{\text{mix}}(D)$ is the mixture NLL of §3.2 (Eq. 3).

Weight-regularization loss. To drive the mixture weights toward the correct regime per pixel, we add

$$\mathcal{L}_{\text{weights}} = \begin{cases} \|\pi_0 - 1\|^2 + \|\pi_1 - 1\|^2, & \text{if pixel } i \text{ is transparent} \\ \|\pi_0 + \pi_1 - 1\|^2, & \text{otherwise.} \end{cases} \quad (30)$$

The first case drives both heads toward full activation, preserving both depth layers; the second recovers softmax-like sum-to-one behavior, so the boundary-aware selection from §3.3 still applies on opaque pixels.

Inference Strategy. At inference, we use the weight sum as a soft transparency indicator: if $\sum_k \pi_k > 1.5$, we treat the pixel as transparent and output both depth predictions as two separate layers; otherwise we treat it as opaque and select a single depth via the component-selection rule of §3.3. This lets the model produce multi-layer depth at transparent pixels while maintaining sharp boundaries at opaque ones.

Initialization, Curriculum, and Optimization. We instantiate the mixture head on the single-view depth estimator DA3MONO-LARGE [13] and use the same symmetry-breaking initialization as the boundary-handling model. Training also follows the same three-stage curriculum, on 4 RTX Pro 6000 GPUs with learning rate $1e-4$ and batch size 128, for a total of 31,000 steps: 1,000 steps for the new mixture projection alone, 5,000 steps with the rest of the DPT head unfrozen (backbone still frozen), and 25,000 steps with the local-attention layers of the backbone additionally unfrozen. Following DA3, the base resolution is 504×504 and training image resolutions are randomly sampled from $\{504 \times 504, 504 \times 378, 504 \times 336, 504 \times 280, 378 \times 504, 336 \times 504, 672 \times 504\}$.

C Additional Experiments

This section reports additional results that complement §5.1 and §5.2 of the main paper. §C.1 contains additional results on boundary and depth quality (multi-view reconstruction, ablations, qualitative comparisons, per-component visualizations, and failure cases). §C.2 contains additional results on the transparent-object and sky-region variants.

C.1 Boundary and Depth Quality

Evaluation Metrics. We use two families of metrics. For **multi-view 3D reconstruction** on NRGBD, 7Scenes, and HiRoom we follow DA3 [13] and report Accuracy (Acc \downarrow ; mean distance from predicted to ground-truth points, in mm), Completeness (Comp \downarrow ; mean distance from ground-truth to predicted points, in mm), and Normal Consistency (NC \uparrow ; cosine similarity of surface normals). Each metric is reported as both mean and median across pixels. For **boundary quality** we follow Pixel-Perfect-Depth [31]: we extract edge masks from the ground-truth depth with the Canny operator (low/high hysteresis thresholds 100/200) and compute Chamfer Distance (CD \downarrow) and Accuracy (Acc \downarrow) in millimeters on the resulting boundary point clouds at two granularities — *per-image* (frame-level) and *per-sequence* (scene-level, aggregating point clouds across frames in a sequence). To remove depth-scale bias, we align predictions to the ground truth before evaluation: for methods that DA3, VGGT, and Ours, we fit a single global scale per sequence; for PPD and PPVD, we instead fit a per-frame scale and shift, which gives them the benefit of optimal local alignment. We emphasize Acc on boundary point clouds because it directly penalizes flying points: a point in the empty space between foreground and background lies far from *both* surfaces, so its predicted-to-GT distance grows with the foreground–background gap and is not absorbed by either alignment.

Table 4: Multi-view 3D reconstruction. Our method stays on par with DA3 and VGGT and substantially outperforms PPD/PPVD across datasets.

Method	NRGBD						7Scenes						HiRoom					
	Acc↓		Comp↓		NC↑		Acc↓		Comp↓		NC↑		Acc↓		Comp↓		NC↑	
	Mean	Med.	Mean	Med.	Mean	Med.	Mean	Med.	Mean	Med.	Mean	Med.	Mean	Med.	Mean	Med.	Mean	Med.
PPD [31]	45.0	27.0	22.0	10.0	0.855	0.978	34.0	20.0	33.0	18.0	0.795	0.908	58.0	37.0	19.0	9.0	0.820	0.963
PPVD [32]	96.0	52.0	29.0	16.0	0.726	0.845	43.0	27.0	36.0	18.0	0.717	0.819	116.0	69.0	29.0	13.0	0.705	0.825
VGGT [24]	20.0	13.0	15.0	<u>6.0</u>	0.882	0.988	29.0	16.0	29.0	16.0	0.764	0.878	28.0	18.0	15.0	<u>7.0</u>	0.859	<u>0.985</u>
DA3 [13]	10.0	5.0	11.0	4.0	0.948	0.995	24.0	<u>13.0</u>	27.0	14.0	<u>0.805</u>	<u>0.917</u>	11.0	6.0	8.0	4.0	0.919	0.993
VGGT + Ours (GMM)	16.0	10.0	15.0	<u>6.0</u>	0.886	0.988	24.0	<u>13.0</u>	25.0	13.0	<u>0.805</u>	0.913	24.0	15.0	14.0	<u>7.0</u>	0.855	0.982
DA3 + Ours (LMM)	12.0	<u>7.0</u>	11.0	4.0	0.904	0.987	22.0	11.0	23.0	11.0	0.791	0.901	13.0	<u>8.0</u>	8.0	4.0	0.869	0.980
DA3 + Ours (GMM)	<u>11.0</u>	<u>7.0</u>	<u>12.0</u>	4.0	<u>0.912</u>	<u>0.990</u>	<u>23.0</u>	11.0	<u>25.0</u>	<u>12.0</u>	0.811	0.918	14.0	<u>8.0</u>	<u>9.0</u>	4.0	<u>0.878</u>	<u>0.985</u>

Table 5: Ablation on the number of mixture components K . All settings with $K \geq 4$ yield comparable full-cloud and boundary quality.

Method	NRGBD						HiRoom					
	CD↓	Video		Image		CD↓	Video		Image			
		Boundary	CD↓	Boundary	CD↓		Boundary	CD↓	Boundary	CD↓		
Ours $K=2$	<u>11.5</u>	<u>31.5</u>	<u>36.0</u>	11.5	<u>29.5</u>	<u>36.0</u>						
Ours $K=4$	<u>11.5</u>	30.5	35.0	11.5	28.0	34.0						
Ours $K=6$	10.5	<u>31.5</u>	37.5	11.5	<u>29.5</u>	37.5						
Ours $K=8$	12.5	33.0	38.0	<u>12.0</u>	35.0	44.5						

C.1.1 Experimental Results

Multi-View Reconstruction. Following DA3 [13], we evaluate multi-view 3D reconstruction on NRGBD, 7Scenes, and HiRoom, reporting accuracy (Acc), completeness (Comp), and normal consistency (NC) with both mean and median values. As shown in Table 4, our mixture representation stays on par with the corresponding baseline on all three datasets: DA3+Ours achieves the best completeness on 7Scenes and HiRoom and the best or second-best accuracy on HiRoom, while remaining within a small margin on NRGBD. This confirms that the boundary improvements reported in the main paper come at little cost to standard scene reconstruction.

C.1.2 Experimental Analysis

Ablation: Number of Components. Table 5 varies the number of mixture components $K \in \{2, 4, 6, 8\}$. All settings with $K \geq 4$ yield comparable full-cloud and boundary CD, indicating that a small handful of components is already sufficient to capture the bimodal geometry at occlusion boundaries; further increasing K does not provide consistent gains and slightly hurts boundary quality on HiRoom at $K=8$. We therefore adopt $K=4$ as the default, since it matches the accuracy of larger K while using fewer head parameters.

Ablation: Inference Strategy. In §3.3 we adopt the *component-selection* rule at depth inference: the mixture density is evaluated at each component’s mode, and the component with the largest value is returned as the point prediction. We compare it against two alternatives in Table 6. (i) *Mixture argmax* takes the argmax of the continuous mixture density directly. The two rules approximately coincide when the components are well-separated and yield near-identical boundary scores, but the continuous argmax requires per-pixel numerical optimization, making it much slower than the mode-selection variation. (ii) *Expectation* decodes the mixture by its mean, $\mathbb{E}[\hat{D}] = \sum_k \pi_k \hat{D}_k$. At a boundary pixel, the expectation lands in the empty space between the surfaces, recreating the flying-point failure. The boundary scores for this strategy are much times worse than those of mode selection. We therefore adopt mode selection as the default.

C.1.3 Extra Qualitative Results

Boundary Comparisons. Figure 14 expands the boundary comparison of Figure 5 in the main paper. Each row shows the input image and results generated by the DA3 baseline, the VGGT baseline, PPD, and our model. Across every scene, the three baselines generate many flying points

Table 6: Ablation on inference strategy. Mode selection (our default) and Mixture argmax give nearly identical boundary scores, but mode selection runs roughly $2\times$ faster. Decoding the mixture by its expectation performs much worse since it averages the foreground and background hypotheses and generates flying points.

Strategy	NRGBD				HiRoom				FPS \uparrow
	Img		Seq		Img		Seq		
	Acc \downarrow	CD \downarrow	Acc \downarrow	CD \downarrow	Acc \downarrow	CD \downarrow	Acc \downarrow	CD \downarrow	
Mode selection (default)	25.0	35.0	24.0	30.5	31.0	34.0	30.0	28.0	33.32
Mixture argmax	26.0	35.5	24.0	30.5	31.0	34.0	30.0	28.0	14.52
Expectation	114.0	90.0	101.0	76.0	67.0	54.0	62.0	45.0	34.50

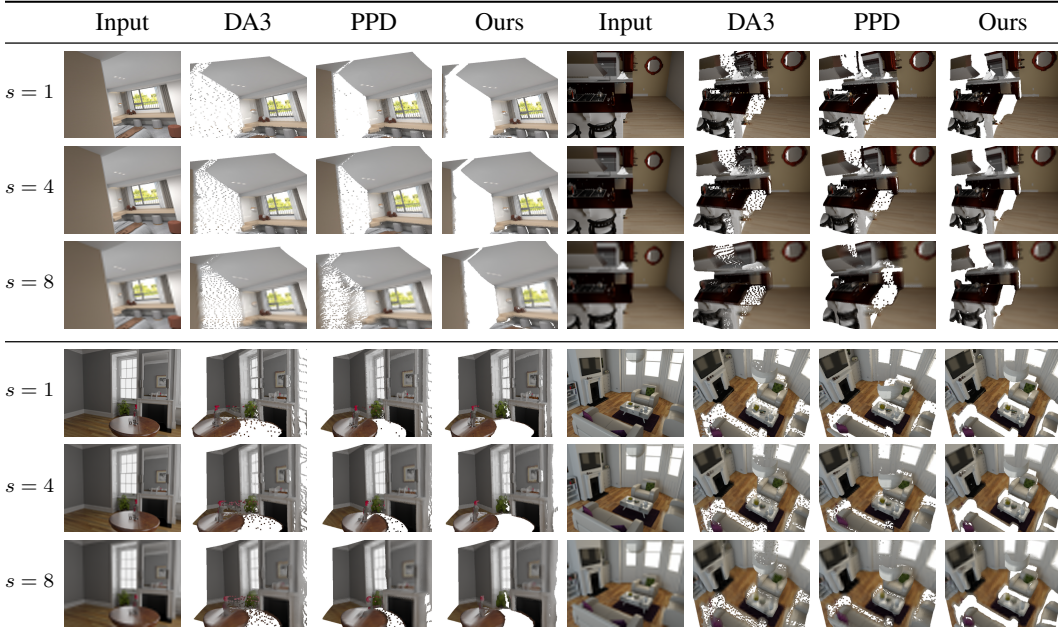


Figure 9: Additional qualitative boundary reconstruction under input blur. As s grows, the baselines (DA3, PPD) develop progressively thicker bands of flying points along surface boundaries, while our mixture-density head keeps the foreground/background separation sharp across all blur levels.

across object boundaries — along chair legs, table edges, doorways, and human silhouettes — while our mixture head preserves clean boundary geometry.

Per-Component Visualizations. Figure 15 visualizes the individual depth maps and mixture weights predicted by each of the K components. At boundary pixels, different components capture the foreground and background surfaces separately, while in smooth regions the components converge to similar depths with one dominant weight — matching the qualitative behavior predicted by the mixture representation in §3.2.

Boundary Reconstruction Under Blur. Figure 9 provides additional qualitative results for the blur-robustness experiment of §5.1 (Figure 7 in the main paper). The unimodal baselines accumulate thicker flying-point bands as s grows, because weaker boundary evidence forces a larger compromise between the two surfaces under a single-mode prediction. Our mixture head keeps each component anchored to one surface (foreground or background), so the predicted boundary stays sharp even at $s=8$, consistent with the gradient-gating analysis of §A.4.

Table 7: Transparent object depth on the LayeredDepth synthetic validation set. Our model outperforms both DA3 and DA3-Multilayer baselines.

Method	First Layer		Last Layer		Boundary Acc↓		Boundary CD↓	
	AbsRel↓	$\delta < 1.25$ ↑	AbsRel↓	$\delta < 1.25$ ↑	First	All	First	All
DA3 [13] (monocular)	0.158	0.771	0.290	0.546	80.4	72.0	89.8	131.1
DA3-Multilayer (monocular)	0.118	0.872	0.202	0.734	72.9	75.5	81.1	95.6
Ours (monocular, LMM)	0.107	0.879	0.213	0.718	59.9	70.3	74.0	90.3
Ours (monocular, GMM)	0.100	0.896	0.182	0.758	60.1	68.8	71.7	90.6

Table 8: Multi-layer depth ordering on the LayeredDepth real-world validation set with human annotations.

Method	Pairs ↑	Triplets ↑	Quadruplets ↑
DA3 [13] (monocular)	0.697	0.583	0.301
DA3-Multilayer (monocular)	0.790	0.576	0.289
Ours (monocular, LMM)	0.935	0.677	0.304
Ours (monocular, GMM)	0.907	0.715	0.302

C.2 Experiments on Extensions

Evaluation Metrics. For **transparent object depth** on the LayeredDepth benchmark [30] we follow the protocol of Wen et al. [30]. On the synthetic validation set we report AbsRel (↓) and $\delta < 1.25$ (↑) for the first (visible) and last (occluded) depth layers, and edge-aware boundary Accuracy (Acc; ↓, mm) and Chamfer Distance (CD; ↓, mm) computed on the first layer alone and across all layers. On the real-world validation set, which provides human-annotated multi-layer depth orderings, we report ordering accuracy (↑) at three granularities — pairwise, triplet, and quadruplet. For **sky estimation** on Sintel we report sky-segmentation IoU (↑) computed against the Sintel semantic-segmentation ground truth, using the sky mask obtained by argmax over the mixture weights (§4.2).

C.2.1 Transparent Object Depth

We evaluate multi-layer depth estimation on the LayeredDepth benchmark [30], which provides a synthetic validation set and a real-world validation set with human annotations.

Synthetic. Following [30], on the synthetic validation set we report AbsRel and $\delta < 1.25$ accuracy for the first and last depth layers, and we additionally report edge-aware boundary Accuracy (Acc) and Chamfer Distance (CD) to quantify how cleanly transparent surfaces are reconstructed (Table 7). Our sigmoid-weighted mixture formulation improves over the DA3 baseline on every column. The gains hold against a stronger DA3-Multilayer baseline that predicts two depth layers without the mixture loss, confirming that multi-layer recovery and clean transparent-surface boundaries are driven by the mixture loss.

Real-World. The real-world validation set provides human-annotated multi-layer depth orderings. Following the protocol of [30], we report pairwise, triplet, and quadruplet ordering accuracy in Table 8. Our method improves markedly on pairs (0.697→0.935) and triplets (0.583→0.715) over the DA3 baseline. The DA3-Multilayer variant, which adds a second depth head without the mixture loss, captures only part of this gain.

Qualitative Examples. Figure 10 shows additional multi-layer predictions on real LayeredDepth scenes, expanding on the two examples in Figure 8a of the main paper.

C.2.2 Sky Estimation

Quantitative. We evaluate the dedicated sky component on Sintel sequences (only three sequences have a clear and separable sky: `alley_2`, `temple_2`, `temple_3`). Table 9 reports sky-segmentation

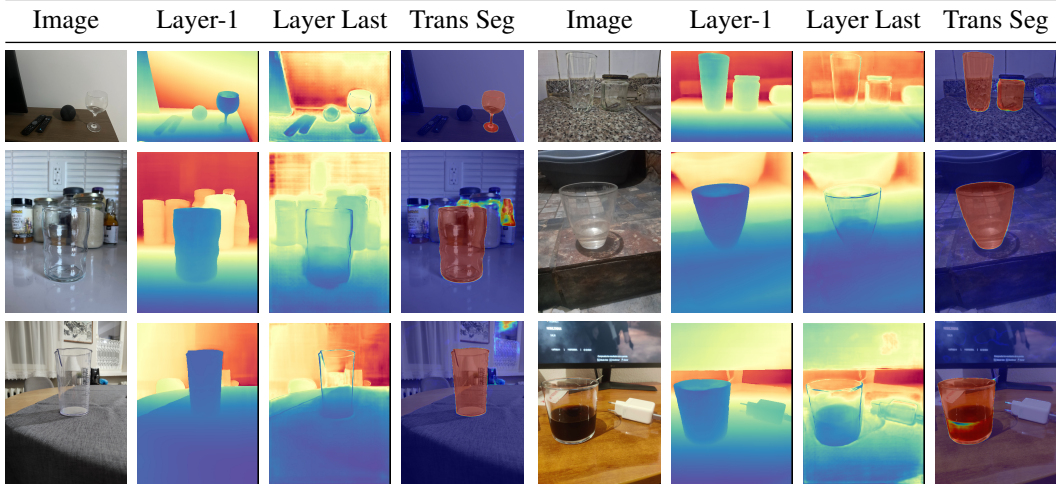


Figure 10: Qualitative multi-layer depth on the LayeredDepth real-world set [30]. For each scene we show, left to right: the input image, the predicted first depth layer (visible transparent surface), the predicted last depth layer (occluded geometry behind it), and the transparency segmentation derived from the mixture-weight sum (§4.1).

Table 9: Sky segmentation on three outdoor Sintel sequences. “DA3-nested” uses the dedicated sky-segmentation network shipped alongside DA3 [13]; “Ours” produces threshold-free sky masks from the dedicated sky component (§4.2) by argmax over mixture weights, without any additional segmentation head or auxiliary supervision.

Method	alley_2	temple_2	temple_3
DA3-nested [13]	0.961	0.823	0.715
Ours	0.951	0.826	1e-5

IoU obtained from the sky component’s argmax (§4.2) and compares against the dedicated sky-segmentation network shipped alongside DA3 [13].

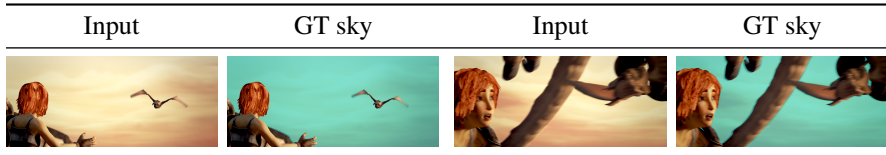


Figure 11: Two representative frames from Sintel `temple_3`: the input RGB and the ground-truth sky mask (green = sky). Sky pixels dominate most of the frame — a sky-dominant configuration that does not appear in our synthetic training mix — which explains the near-zero IoU on this sequence reported in Table 9.

The near-zero IoU on `temple_3` in Table 9 is a training-distribution artifact rather than a failure of the formulation. As Figure 11 illustrates, sky pixels occupy most of the frame in this sequence — a sky-dominant configuration that does not appear in our synthetic training mix. DA3’s nested sky-segmentation network does not disclose its training data, but is presumably trained on a substantially more diverse image distribution that includes such scenes. We expect this gap to close given comparable training coverage of sky-dominant outdoor data, and we leave a more comprehensive sky-training mix to future work.

Qualitative Examples. Figure 12 shows additional sky-handling comparisons (input / baseline / ours) on Sintel sequences, expanding on the two examples in Figure 8b of the main paper.

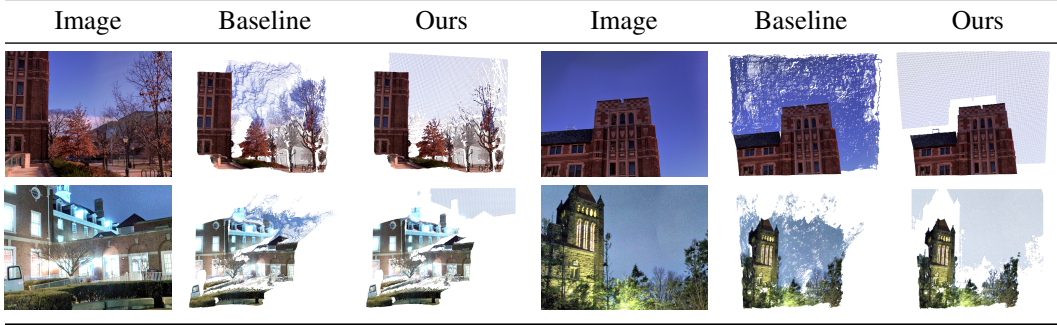


Figure 12: Qualitative comparison on sky regions. Without a dedicated sky component, the baseline produces flying points along the entire skyline; our model assigns sky pixels to the sky component, producing clean sky boundaries.

D Failure Cases and Limitations

Figure 13 highlights two characteristic failure modes of our mixture representation. *First* (Figure 13, left), although our method produces far fewer flying points than prior approaches, occasional some depth artifacts still appear on object surfaces oriented nearly parallel to the camera viewing direction. At such grazing angles the appearance cue degenerates — a small image patch projects to a long range of depths, so some artifacts still occasionally appear on these surfaces. *Second* (Figure 13, right), we inherit the failure modes of the DA3 backbone itself: depth predictions on small thin structures are locally distorted. Since our model is finetuned from the DA3 checkpoint, it is hard to rescue these predictions.

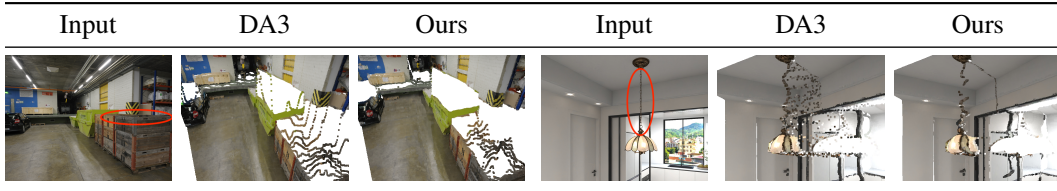


Figure 13: Failure cases. *Left*: Although our method produces far fewer flying points than the baselines overall, depth artifacts still appear on surfaces oriented nearly parallel to the camera viewing direction, where the grazing-angle appearance gives weak depth cues. *Right*: We inherit failure modes of the DA3 backbone: depth on small thin structures is locally distorted.

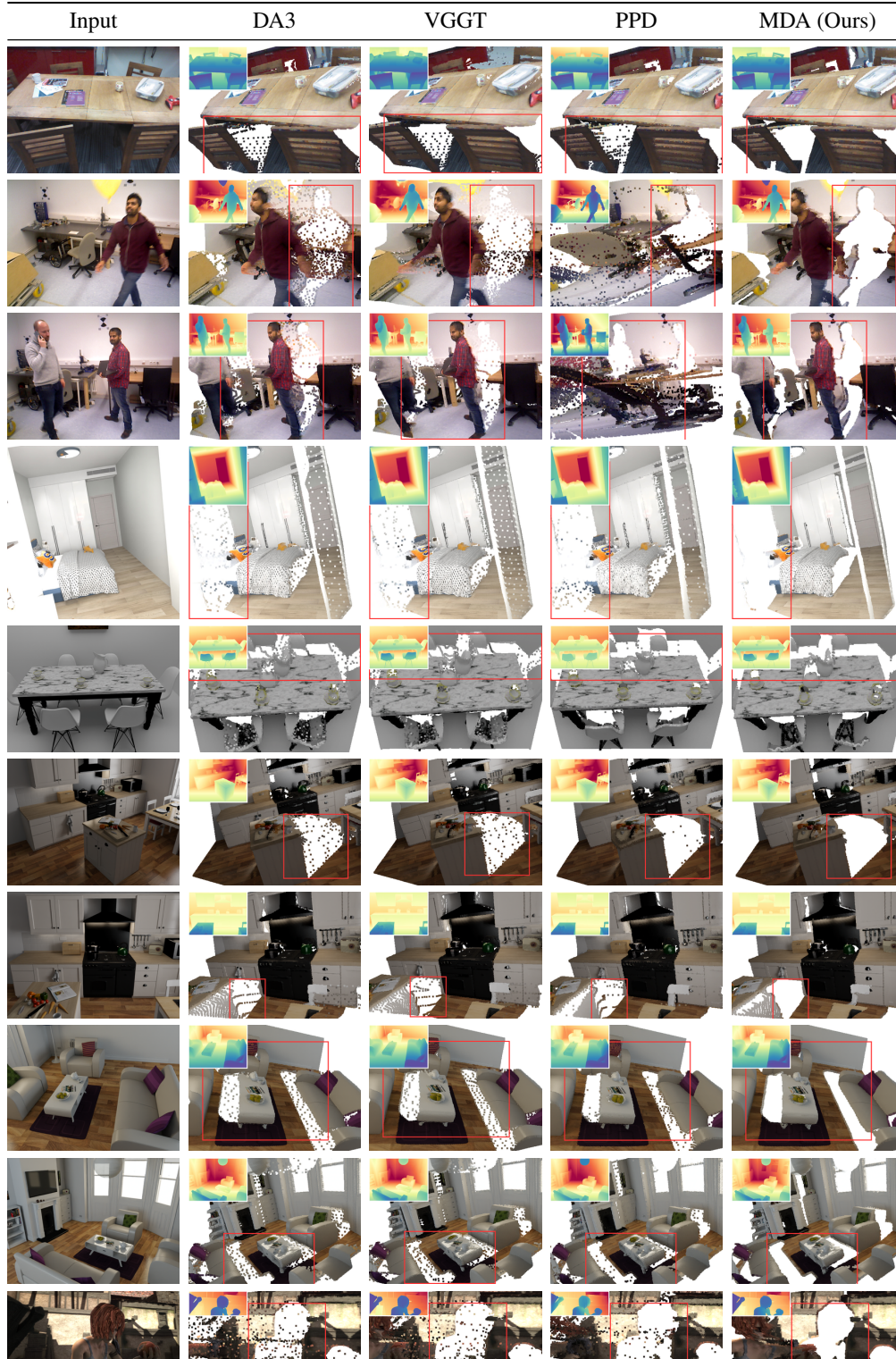


Figure 14: Additional qualitative boundary comparison across nine scenes drawn from 7Scenes, Bonn, HiRoom, NRGBD, and Sintel. Baseline methods (DA3, VGGT, PPD) leave visible flying points wherever depths differ sharply, while our approach keeps the boundary clean across all scenes.



Figure 15: Per-component visualization of heads with $K=4$. For each scene, the leftmost column shows the input image (top) and our final fused depth (bottom); the four right columns show the per-pixel mixture weight π_k (top) and the corresponding component mean depth D_k (bottom). Components specialise spatially: at occlusion boundaries different heads lock onto the foreground and background surfaces, whereas in smooth regions one head carries almost all the weight while the others converge to similar depths.